# Ferroelectric-Based Catalysis: Switchable Surface Chemistry
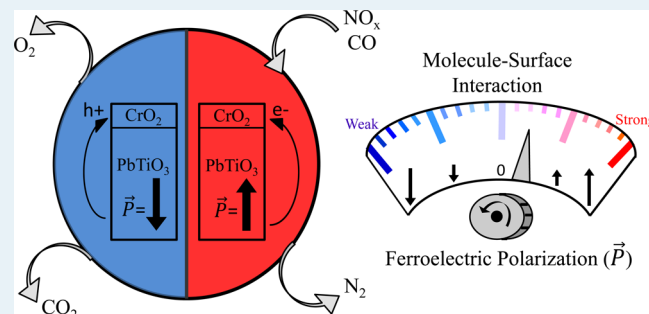
Arvin Kakekhani*,[†] and Sohrab Ismail-Beigi[†,‡,§,⊥]

[†]Department of Physics, [‡]Department of Applied Physics, [§]Department of Mechanical Engineering and Materials Science, [⊥]Center for Research on Interface Structure and Phenomena (CRISP), Yale University, New Haven, Connecticut 06520, United States

Ⓢ Supporting Information

**ABSTRACT:** The maximum efficiency of a fixed catalytic surface occurs when the adsorbate−surface interaction strength is optimal as per the Sabatier principle: strong enough to drive the reactions forward but weak enough to permit the products' desorption. Such a compromise can fundamentally limit catalytic activity. One solution is to create a surface with switchable activity between strong binding (rapid dissociation) and weak binding (easy desorption). On the basis of first-principles theory, we describe a class of catalysts comprising an epitaxial monolayer of a transition metal oxide on an oxide ferroelectric substrate in which reversing the ferroelectric polarization state switches the



surface activity between these two limits. As an example, a $CrO_2$ monolayer on ferroelectric $PbTiO_3$ permits direct $NO_x$ decomposition and CO oxidation while circumventing oxygen and sulfur poisoning. Our computed binding energy trends are explained by a generalization of the canonical d-band model for transition metals to metal oxide surfaces combined with charge transfer effects.

**KEYWORDS:** ferroelectric-based catalysis, ferroelectric surfaces, direct $NO_x$ reduction, CO oxidation, density functional theory, metal oxide surface chemistry, surface oxidation state

## INTRODUCTION

In agreement with the Sabatier principle, the plot of catalytic activity versus molecular adsorption strength for a variety of catalytic surfaces shows a maximum at an intermediate binding strength: a "volcano plot".[1−3] Sensibly, much effort in catalyst design aims to find surfaces whose binding energetics are "just right" for the molecules involved in key steps of a reaction.[4−8]

A priori, it would be desirable to have a single surface whose activity is tunable, via external control of an order parameter, from strong binding and rapid dissociation to weak binding and easy desorption. One possibility is the surface electron density: for example, the surface chemistry of $SnO_2$ nanowires[9,10] or graphene[11] is controllable using a gate voltage that alters the electron density. An alternative is a ferroelectric surface: when the ferroelectric has an out-of-plane polarization (i.e., electrical dipole density) $\vec{P}$, there is a surface charge density $\vec{P} \cdot \hat{n}$ which must be compensated by changes in the surface charge density. Switching the direction of the polarization changes the surface's electronic states[12−14] and can promote specific reactions. Previous work has highlighted the potential benefit of depositing a monolayer of a transition metal oxide on a ferroelectric surface for enhancing surface reactivity.[15] As we describe below, these active monolayers can overcome the thermodynamic stability problems that have hindered prior applications of similar ideas: for example, transition metal layers, while chemically active in theory, do not wet ferroelectric surfaces but instead aggregate to form bulklike nanoparticles.[16−19] We show that the oxide monolayers we propose, when used in a mode where the

polarization is flipped cyclically, lead to enhanced catalytic behavior that is not limited to an intermediate range of adsorbate−substrate interaction strength (i.e., the Sabatier principle) but instead takes advantage of both sides of the volcano. This approach is general and can be applied to a variety of reactions. We demonstrate its utility for simultaneous direct decomposition of $NO_x$ (i.e., NO and $NO_2$) into $N_2$ and $O_2$[20−28] and CO oxidation into $CO_2$. Both reactions are critical in the automotive emission control industry.[23,25,26,29,30]

The potential of ferroelectrics to enhance surface chemistry and catalytic behavior is a subject that has been studied experimentally for more than six decades.[17,31−44] A number of first-principles theoretical works have become available in the past decade.[15,16,19,43,45,46] Thus far, efforts in this field have examined bare or modified ferroelectric surfaces with fixed polarization and have exploited the ferroelectric polarization to optimize adsorbate interaction energies toward the top of the volcano; hence, they have remained loyal to the main idea of the Sabatier principle. Interestingly, Kim et al. studied Pd on ferroelectric $LiNbO_3$ and described the "intriguing possibility" that the activity of the catalytic Pd layer could be modulated by switching the polarization, but in the end dismissed this possibility because Pd does not wet the surface but instead

aggregates to form large clusters on LiNbO$_3$ and, thus, only weakly couples to the ferroelectric substrate.[19]

In this work, for the first time, we quantitatively show how one can use the ferroelectric polarization in a cyclic manner while simultaneously exploiting the thermodynamical driving force for reconstructions of the ferroelectric surfaces[15,47−50] to efficiently drive desired reactions and create a complete catalytic cycle. This new approach can bring us beyond the limits of the Sabatier principle. We describe a class of systems that could be optimized to perform a wide range of reactions and that, unlike transition metal thin films on ferroelectrics,[16,17,19] are thermodynamically stable and thus, in principle, can be fabricated experimentally.

## ■ RESULTS AND DISCUSSION

The fact that bulk RuO$_2$ catalyzes NO decomposition[51,52] motivates us to place a RuO$_2$ monolayer on the (001) PbO-terminated PbTiO$_3$ (PTO) surface, which is its thermodynamically stable termination.[15,53,54] Table 1 displays first-principles

**Table 1. Polarization-Dependent Binding Energies in eV for Intact and Dissociated Molecules Involved in NO$_x$ Direct Decomposition on RuO$_2$−PbTiO$_3$ and CrO$_2$−PbTiO$_3$ for Positive, Paraelectric and Negative Polarizations, Indicated by (+), (0), and (−), Respectively, for 0.5 Monolayer (ML) Coverage**[a]

| binding molecule | mode | RuO$_2$−PTO + | 0 | − | CrO$_2$−PTO + | 0 | − |
|---|---|---|---|---|---|---|---|
| NO | intact | 2.0 | 1.8 | 1.3 | 1.9 | 1.9 | 0.1 |
| | N + O | 1.2 | 0.3 | −1.4 | 2.5 | 1.5 | NS |
| NO$_2$ | intact | 1.8 | 1.7 | 1.1 | 1.9 | 1.6 | −0.1 |
| | NO + O | 2.0 | 1.7 | 0.4 | 3.2 | 2.4 | NS |
| O$_2$ | intact | 1.6 | 0.9 | 0.2 | 1.2 | 1.8 | 0.3 |
| | O + O | 2.0 | 1.1 | −0.7 | 4.5 | 4.2 | −0.2 |
| N$_2$ | intact | 0.1 | 0.6 | 0.3 | 0.2 | 0.2 | 0.0 |

[a]More positive numbers denote increased stability. Binding energies are relative to the energy of the gas phase molecules. NS means no mechanically stable configuration exists. Negative values indicate mechanically stable metastable states (local minima) that are less stable than the gas phase molecules.

calculated results for the polarization-dependent binding energies for a number of molecules on RuO$_2$-terminated PTO. In this work, more positive binding energies indicate more energetically stable configurations. Positive polarization (along the surface normal vector) leads to extra electrons appearing on the surface to compensate the surface charge density ($\vec{P}\cdot\hat{n}$): this creates the strong interaction regime sporting large binding energies. Negative polarization adds extra holes to the surface and pushes the surface to the weak-binding, desorptive regime in almost all cases. Encouraged by this, we calculate the NO dissociation, N$_2$ formation, and O$_2$ dissociation barriers in positive polarization and present them in Table 2. The tables show that for positive polarization, (i) O$_2$ molecules readily dissociate into bound O atoms, (ii) a fraction of the NO molecules will dissociate into bound N and O atoms, and (iii) the small N$_2$ formation barrier means that resulting N atoms readily form N$_2$—instead of reforming NO—which is weakly bound and leaves the surface. Up to this point, some NO molecules have dissociated, but the surface has become saturated by strongly bound O atoms (i.e., oxygen inhibition), a standard problem in NO direct decomposition catalysis.[55−60] Switching the polar-

**Table 2. Energy Barriers in eV for Key Reactions on Positively Poled CrO$_2$−PbTiO$_3$ and RuO$_2$−PbTiO$_3$**[a]

| reaction | CrO$_2$−PTO | RuO$_2$−PTO |
|---|---|---|
| NO dissociation | 0.9 | 1.3 |
| O$_2$ dissociation | 0.0 | 0.0 |
| NO$_2$ dissociation | 0.5 | 0.0 |
| N$_2$ formation | 1.2 | 0.5 |
| CO$_2$ formation | 1.6 | 0.8 |

[a]The energy barriers are defined as the energy difference between the transition state (located by NEB method with climbing image) and the adsorbed (chemisorbed) reactants state.

ization at this point strongly destabilizes the bound atomic O: the O atoms form O$_2$, which is bound weakly and desorbs easily. This returns us to a pristine surface that is ready for the next polarization cycle.

We envision operating the system in a cyclical manner by repeatedly switching polarization between a reducing surface ($P > 0$) and an oxidizing surface ($P < 0$). After each switch, the surface finds itself in a high-energy state and tries to reach its thermodynamic ground state whose stoichiometry and structure can be predicted from first principles.[15,61,62] However, in the process of this evolution, it must pass through the chemically active stoichiometric structures that we focus on in this work: we are, in fact, leveraging this surface evolution to drive the desired reactions. For example, as described above, the stoichiometric positively poled surface dissociates O$_2$ and NO molecules and is driven to be saturated with strongly bound O atoms. This O-rich surface is the thermodynamic ground state and is less chemically reactive. Switching to negative polarization then cleans off these O atoms (via O$_2$ formation and desorption), and the surface becomes stoichiometric, which is again at or near its thermodynamic ground-state for negative polarization and is ready for the next polarization flip.

Of course, there is no a priori reason why a monolayer of RuO$_2$, quite far from bulk RuO$_2$, is necessarily optimal; hence, we optimize the choice of transition metal oxide monolayer to (i) minimize the NO dissociation barrier, (ii) maximize the NO reformation barrier, and (iii) preserve the small N$_2$ formation and desorption barriers in the positive polarization state while (iv) enhancing inertness in the negative polarization state to ensure maximum desorption power and deliver a pristine surface. We have considered a number of d-block transition metals, including Ru, W, Mo, Fe, Cr, Pt, Au, and Cu. We find that, beginning from Ru, moving to the left or downward on the periodic table increases the interaction with NO and the O$_2$ formation barrier while decreasing the NO dissociation barrier, and moving to the right or upward has the opposite effect. Mo and W interact too strongly with the adsorbates, and Fe, Pt, Au, and Cu interact too weakly (further details can be found in the Supporting Information).

We find that Cr is optimal for our needs. Table 1 lists binding energies for the CrO$_2$−PTO surface. Positively poled CrO$_2$−PTO is highly active toward adsorbates, whereas the negatively poled surface is almost inert. Unlike RuO$_2$−PTO, the ground state for NO in positive polarization is to be dissociated into bound N and O atoms. Similarly, dissociated NO$_2$ (NO + O) is favored over the intact molecule in positive polarization (see Table 1) with a small dissociation barrier as per Table 2 (the NO will further dissociate into N and O atoms). Eventually, the bound N and O atoms are converted to N$_2$ and O$_2$ in later steps of the cycle. Table 2 provides the key barriers on positively poled

$CrO_2$−PTO: the NO dissociation barrier has been lowered compared with $RuO_2$−PTO, the $O_2$ dissociation barrier is negligible, and the $N_2$ formation barrier is somewhat increased. We graphically illustrate our envisioned cycle in Figure 1 showing
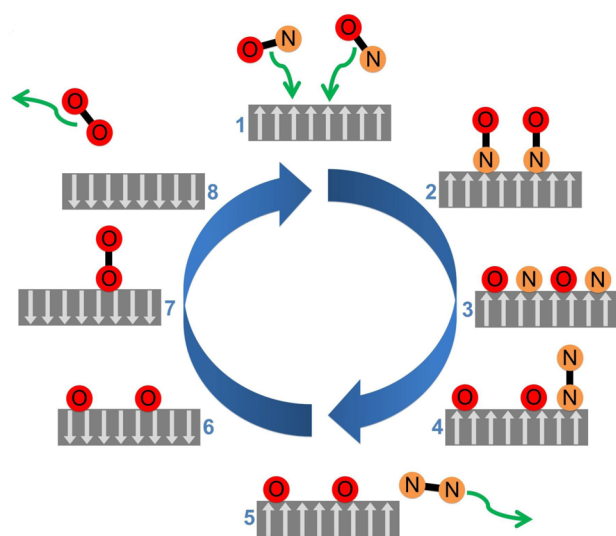


**Figure 1.** Proposed catalytic cycle on $CrO_2$−$PbTiO_3$ for NO direct decomposition into $N_2$ and $O_2$. In each case, the polarization direction is indicated by gray arrows. The green arrows show adsorption and desorption of the molecules. The cycle is begun from a clean and pristine positively poled surface and, through multiple steps (after effectively dissociating 2 NO molecules into $N_2$ and $O_2$), returns to this state.

how cyclical polarization switching of $CrO_2$−PTO can effectively catalyze NO direct decomposition into $N_2$ and $O_2$. The energy landscape diagram of the cycle is depicted in Figure 2, where we can see the progression of surface states and the quantitative changes in energy states, as well as the key transition states.

In addition to $NO_x$ direct decomposition into $N_2$ and $O_2$, both $RuO_2$−PTO and $CrO_2$−PTO can simultaneously oxidize CO into $CO_2$. Table 3 shows that the O-rich positively poled surfaces oxidize CO into $CO_2$, since (a) CO has a strong interaction with the surfaces, (b) $CO_2$ formation is favored over separated CO and O, and (c) $CO_2$ formation barriers are modest in both systems (see Table 2). On $RuO_2$−PTO surfaces, $CO_2$ is released after formation (in positive polarization), whereas on $CrO_2$−PTO, $CO_2$ is released after switching to negative polarization,
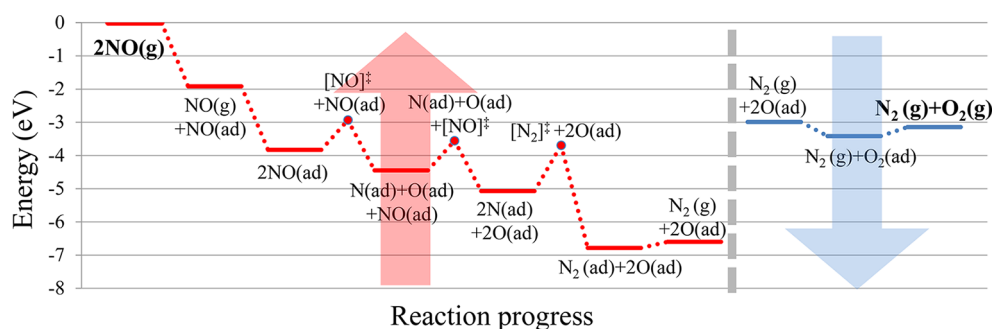
**Table 3. Polarization-Dependent Binding Energies in eV for CO, $CO_2$, $SO_2$ and $H_2O$ on $RuO_2$−PTO and $CrO_2$−PTO for Positive, Paraelectric, and Negative Polarizations, indicated by (+), (0), and (−), Respectively for 0.5 ML Coverage[a]**

| binding molecule | mode | $RuO_2$−PTO | | | $CrO_2$−PTO | | |
|---|---|---|---|---|---|---|---|
| | | + | 0 | − | + | 0 | − |
| CO | intact | 1.7 | 1.7 | 1.7 | 0.8 | 0.7 | 0.0 |
| $CO_2$ | intact | 0.1 | 0.8 | 0.7 | 0.8 | 1.0 | 0.0 |
| | CO + O | −0.4 | −0.8 | −2.0 | −0.2 | −0.7 | NS |
| $SO_2$ | intact | 0.3 | 0.9 | 0.4 | 1.3 | 0.6 | 0 |
| $H_2O$ | intact | 0.4 | 0.7 | 0.7 | 0.5 | 0.5 | 0.1 |

[a]More positive numbers denote increased stability. Binding energies are relative to the energy of the gas phase molecule. NS means no mechanically stable configuration exists.

where there is negligible surface−molecule interaction (see Table 1). As another surprising added benefit, this class of systems shows tolerance against sulfur poisoning, a significant challenge and an active area in emission control research.[63−68] The binding energies in Table 3 for $SO_2$ and $H_2O$ molecules are small in at least one polarization state: when the polarization is cycled, these molecules readily desorb, and the surface does not become saturated (poisoned).

We conclude this section on cyclic catalysis with some comments on two key rates in this system. First, the chemical reactions on the surfaces have energy barriers $\Delta \sim 1$ eV, which at a temperature of $T = 600$ K and assuming a pre-exponential prefactor of $\nu = 5 \times 10^{12}$ Hz in the transition state theory rate $\nu \exp(-\Delta/k_B T)$, gives order of magnitude estimate rates of $\sim 2 \times 10^4$ Hz. The second time scale is that time required to switch the ferroelectric polarization: electrically, this can be accomplished in existing systems with rates of $\sim 10^7 - 10^8$ Hz;[69,70] hence, the ferroelectric switching rate should not be a limiting factor for such a cyclic device, and we expect to derive the full benefit from the polarization-enhanced catalytic activity.

We now address basic aspects of the stability of these monolayers. We find that monolayers of $RuO_2$ and $CrO_2$ on paraelectric PTO can lower their energies via interdiffusion of Ru (Cr) atoms into the PTO as well as by a lack of wetting (i.e., energetic preference to form bulk $RuO_2$ and $CrO_2$). However, once $P \neq 0$, the interdiffusion problem is overcome because it raises the total energy, but the wetting problem remains. One solution involves a simple modification in which $x$ unit cells of



**Figure 2.** Energy landscape diagram for the proposed catalytic cycle on $CrO_2$−$PbTiO_3$ for NO direct decomposition into $N_2$ and $O_2$. The two arrows indicate the direction of the polarization in each part of the cycle: on the left is positive (up) polarization (parallel to the surface normal vector), and on the right is negative (down) polarization (antiparallel to the surface normal vector). The dashed gray line indicates the point in the cycle at which the polarization is flipped. Horizontal plateaus locate local minima, and circles represent transition states as highlighted by the "‡" label. The reference energy is that of two NO molecules in the gas phase above a $2 \times 2$ $CrO_2$−$PbTiO_3$ surface in positive polarization.

SrTiO$_3$ (STO) are inserted between the catalytic monolayer and the PTO, denoted as Ru(Cr)O$_2$−(STO)$_x$−PTO. Our DFT results for $x = 0-5$ show that bulk oxide formation is suppressed by the presence of the STO buffer layer. Crucially, the polarization-dependent surface chemistry is unchanged (binding energies for $x = 1-5$ change at most by 0.3 eV per adsorbate compared with the $x = 0$ case) which stems from our finding that the polarization propagates perfectly through the STO. This is because STO is a strongly polarizable incipient ferroelectric (quantum paraelectric)[71,72] that is further aided by the strain enforced on it by the PTO to render it ferroelectric.[73,74] With STO as a buffer layer, we effectively have a monolayer of either SrRuO$_3$ or SrCrO$_3$ on the surface of the material. The fact that SrTiO$_3$, SrRuO$_3$, SrCrO$_3$, and PbTiO$_3$ are all experimentally known materials with lattice parameters within 3% of each other[75−82] is also consistent with our prediction of the thermodynamical stability of the Ru(Cr)O$_2$−(STO)$_x$−PTO system with respect to formation of bulk RuO$_2$ and CrO$_2$ or interdiffusion in both polarization states.

We turn to electronic-structure analysis to clarify the underlying physical bases of the striking polarization dependent chemistry. First, we examine how the oxidation state of the surface transition metal changes as a function of polarization. We provide evidence of the oxidation state change for the CrO$_2$ monolayer. First and most simply, the average Cr−O bond lengths in positive and negative polarizations are 1.94 and 1.69 Å, respectively. Because the Cr coordination number is unchanged, this correlates directly with increasing oxidation states,[83] as expected from removal of electrons with decreasing surface charge ($\vec{P}\cdot\hat{n}$). Second, according to our calculations (using the Berry Phase method[84,85]) and in agreement with the literature,[86,87] bulk PTO has a ferroelectric polarization magnitude of $P = 93\ \mu C/cm^2$, which corresponds to a surface charge density of 0.87 electrons/Cr, which must be compensated by addition or removal of electrons to or from the surface. As we show below, the electronic states at or near the Fermi energy have primarily Cr 3d character, so the added or removed electrons will be residing on the surface Cr sites. Given that the polarization profile is quite uniform in our films right up to the surface, we expect the full $\approx\pm1$ change of electron number and, hence, oxidation number on each Cr with polarization reversal. Third, monitoring the magnetic moment of the surface Cr provides a more direct measure of the change of oxidation state. CrO$_2$−PTO is effectively a monolayer of perovskite PbCrO$_3$ on TiO$_2$-terminated PbTiO$_3$. For bulk PbCrO$_3$, we find a large exchange splitting and a magnetic moment of 2 $\mu_B$ per Cr as per prior literature:[88] in both bulk PbCrO$_3$ and CrO$_2$, we have Cr$^{4+}$(3d$^2$) with a large exchange splitting that aligns the two 3d electron spins. For CrO$_2$−PTO, we compute magnetic moments of 3.1 $\mu_B$, 2.2 $\mu_B$, and 0.3 $\mu_B$ per Cr for positive, paraelectric, and negative polarizations, respectively. As expected, the paraelectric state agrees closely with the bulk (i.e., unchanged Cr$^{4+}$ oxidation state). For positive polarization, the enlarged magnetic moment of 3.1 $\mu_B$ and the exchange splitting observed in the density of states (see Figure 3) signal the high-spin Cr$^{3+}$(3d$^3$) state. For negative polarization, we have Cr$^{5+}$(3d$^1$), which has negligible exchange splitting and is paramagnetic (see Figure 3). We note that unlike bulk PbCrO$_3$, which is a G-type antiferromagnet,[89,90] positively poled CrO$_2$−PTO prefers ferromagnetism over antiferromagnetism and paramagnetism by 0.15 and 1.5 eV per Cr, respectively. Hence, CrO$_2$−PTO shows a strong magneto-electric effect: it is a paramagnet in negative polarization but a robust ferromagnet in positive polarization (other examples of
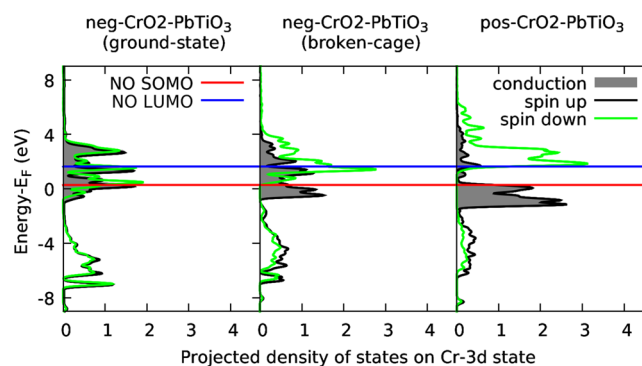


**Figure 3.** Projected density of states (PDOS) on Cr 3d orbitals for CrO$_2$−PbTiO$_3$ in positive and negative polarizations in spin up and down channels. Black lines are majority spin (up) PDOS, and green lines are minority (down) PDOS. The red and blue horizontal lines mark the energies of the SOMO and LUMO states of the NO molecule in gas phase. Left: PDOS on Cr 3d in the ground state for negative polarization (Cr in oxygen tetrahedral cages as per Figure 5a); we see a small exchange splitting that corresponds to one electron per Cr site. Center: PDOS on Cr 3d for the negatively poled surface that is ready for binding adsorbates (oxygen tetrahedral cage is broken as per Figure 5d). Right: PDOS on Cr 3d states for the ground state of the positively poled surface; we see an enlarged exchange splitting that corresponds to the existence of three electrons per Cr site.

ferroelectric control of spin polarization have been discussed in refs[91−97]). In brief, these results show that the polarization can shuttle $\approx\pm1$ electron per surface transition metal, which modifies the oxidation state by $\approx\pm1$ relative to paraelectric case and underpins the dramatic polarization dependent chemistry seen above.

After an extensive analysis, we find that the polarization-dependent surface electron count controls binding energies (Table 1 and 3) via two separate channels: (i) charge transfer between the surface and adsorbates, and (ii) covalent binding between the adsorbates and surface. In most cases, both operate at once, but for simplicity, we present two examples in which one mechanism dominates: (a) charge transfer for O$_2$ dissociative binding and (b) covalent effects for NO intact binding.

Figure 4a,b shows the binding configurations for O$_2$ dissociative binding on RuO$_2$−PTO. As Figure 4e shows, the adsorbate O 2p state is 1.9 eV lower than the surface Fermi energy; hence, the dominant effect is electron transfer from the surface to the oxygen adsorbates. The decrease in the Ru oxidation state (by ∼2 units) is visible as the enlarged occupation of and increase in the density of states of the Ru 4d-dominated conduction bands when changing the sign of $P$. Hence, there is more electron transfer to the low-energy states of the oxygen adsorbate, which greatly increases the binding energy by 2.7 eV per dissociated O$_2$ molecule.

Figure 4c,d shows the binding configurations for NO adsorption on RuO$_2$−PTO. As visible in Figure 4, the tiny difference between the energy of the NO singly occupied molecular orbital (SOMO) and the Fermi energy of the surfaces obviates charge transfer, so covalent bonding between adsorbate and surface states is critical. To understand this, we generalize the well-known d-band model for transition metal surfaces[5] in which the energy difference between the Fermi energy ($E_F$) and the center of the transition metal d band is a good descriptor for adsorption energies. In transition metal oxides, cation d states and O 2p states hybridize to form valence and conduction bands. However, in our systems, (a) molecular binding occurs on the
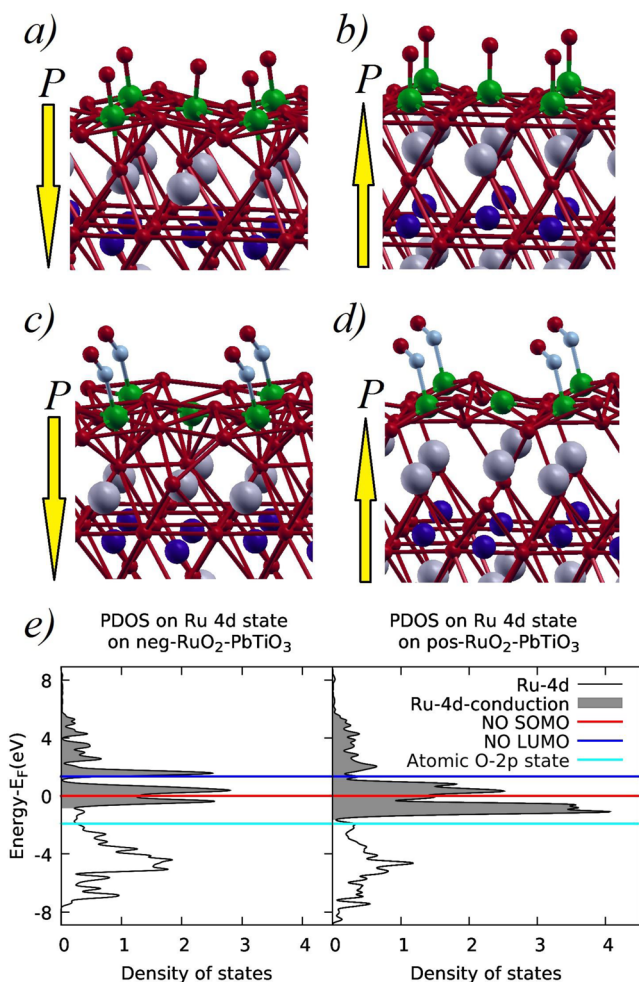
**Figure 4.** Polarization-dependent binding geometries and electronic structure for $RuO_2$–$PbTiO_3$. $O_2$ dissociative binding for (a) negatively and (b) positively poled and NO binding on (c) negatively and (d) positively poled $RuO_2$–PTO. Atoms are Ti (dark blue), Pb (gray), O (red), N (pale blue), and Ru (green).[98] (e) Projected density of states on the surface Ru 4d atomic orbitals for negative and positively poled $RuO_2$–PTO energetically aligned with molecular and atomic adsorbate states. Shaded regions highlight the Ru 4d-dominated conduction bands (for details, see the Methods section).

transition metal sites (e.g., Figure 4), (b) the conduction bands are dominated by antibonding d states, and (c) $E_F$ lies in or near the conduction band, so the obvious generalization is to consider the relative alignment of $E_F$ with the center of the conduction band. Auxiliary reasons are that the portion of the d states that hybridize with O 2p orbitals forming bonding states (i) lie deep in the valence band (well below $E_F$) and do not contribute to adsorbate bonding, and (ii) tend to point in-plane or into the surface and have small spatial overlap with adsorbate molecular orbitals. Figure 4e highlights the alignment of the Ru 4d states with the NO SOMO and lowest unoccupied molecular orbital (LUMO). We compute the center of conduction part of the d band by integrating the shaded Ru 4d portion of the density of states in Figure 4e and find that for $P > 0$, it is closer to the NO SOMO by 0.8 eV ($E_F$ and the SOMO are energetically coincident). Hence, we believe that the energy difference between $E_F$ and the center of the conduction band is a good descriptor of the substrate–adsorbate interaction, especially when covalency is the dominant mechanism in the binding.

The $CrO_2$–PTO system shows very similar behaviors: for negative polarization, we have reduced electron density and an upward shift of the conduction band center relative to Fermi energy when compared with positive polarization, as per Figure 3. As can be seen in Figure 3, the center of the conduction band for positively poled $CrO_2$–PTO lies almost at $E_F$, but the center of the conduction band for negatively poled $CrO_2$–PTO (which is prepared for molecular binding) lies 0.95 eV above the Fermi energy. This leads to a weaker covalent bond between the NO molecule and the surface in negative compared with positive polarization.

Tables 1 and 3 show that the negatively poled $CrO_2$–PTO surface is strikingly inert to molecular interactions. The primary reason for this behavior is geometrical. Figure 5a shows that for
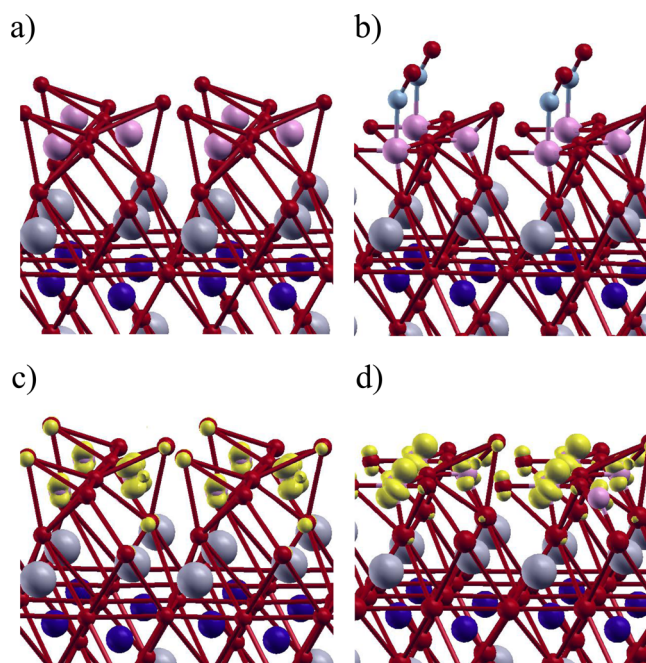


**Figure 5.** Breaking of the oxygen tetrahedral cages upon molecular binding and exposure of Cr 3d states. Surface of negatively poled $CrO_2$–PTO (a) without NO and (b) with NO adsorbed. (c) Local density of states at the Fermi level (yellow isosurfaces) for the ground-state structure of negatively poled $CrO_2$–PTO. The density is localized primarily on the Cr inside the oxygen tetrahedral cages. (d) Local density of states at the Fermi level for the negatively poled $CrO_2$–PTO surface with broken oxygen cages and, hence, exposed Cr that is ready for binding adsorbates. The atoms are Cr (pink), O (red), Pb (gray), and Ti (blue).

the ground state of negatively poled $CrO_2$–PTO, the $Cr^{5+}$ ions are enclosed in distorted tetrahedral oxygen cages. The active electronic states on the surface, which are predominantly on the Cr, are thus inside the cage (see Figure 5c). To bind an adsorbate, a cage must break to expose a Cr, as exemplified by Figure 5b, which then exposes the electronic states at the Fermi level on the Cr to the adsorbate for covalent binding (see Figure 5b,d). Energetically, each cage-breaking costs a penalty of 0.8 eV, destabilizing molecular binding significantly. This unusual behavior likely stems from two sources: First, $Cr^{5+}$ has a single 3d electron, so it prefers maximum local symmetry reduction and a lowest-energy nondegenerate electronic configuration. Second, $Cr^{5+}$ has a relatively small size: we find that isoelectronic $Mo^{5+}$ and $W^{5+}$ do not form such tetrahedral cages. This correlates to

their larger ionic radii ($Mo^{5+}$, 0.61 Å; $W^{5+}$, 0.62 Å; $Cr^{5+}$, 0.49 Å), so they likely do not fit inside a stable $O^{2-}$ tetrahedral cage.[83]

We conclude our analysis of electronic behavior by illustrating the redistribution of electrons in real space upon NO adsorption on positively polarized $CrO_2$−PTO (see Figure 6). We see that
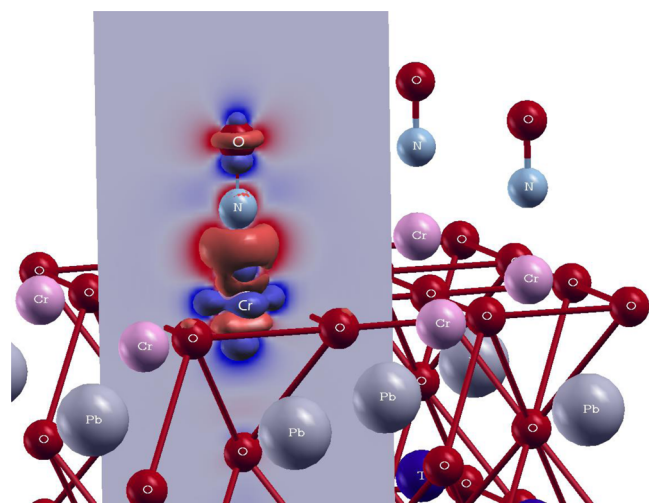


**Figure 6.** Real space electron redistribution shows covalent bond formation upon NO adsorption on the surface Cr atom for positively poled $CrO_2$−PTO. Blue isosurfaces show regions in space that are depopulated by electrons, and red isosurfaces show the regions that get populated by electrons when NO binds to the surface Cr. The state becoming occupied is a bonding combination of the NO SOMO ($\pi$ symmetry) and the surface Cr $3d_{xz}$ and Cr $3d_{yz}$ orbitals.

electrons occupy a bonding state that is a hybrid of the NO SOMO, Cr $d_{xz}$ and Cr $d_{yz}$ states. The states near the edge of the conduction band on the surface Cr atom are made of $d_{xz}$, $d_{yz}$, $d_{xy}$, and $d_{3z^2-r^2}$ orbitals, but the last two do not interact with the NO SOMO, which has $\pi$ character: the $d_{xy}$ orbital points in-plane, whereas the $d_{3z^2-r^2}$ has zero total overlap with NO SOMO by symmetry. Hence, we expect electron transfer from Cr $d_{xy}$ and $d_{3z^2-r^2}$ orbitals to the lower-energy bonding combination of the NO SOMO and Cr $d_{xz}$ + $d_{yz}$ states, which is visible in Figure 6. Covalent bonding of a similar form also takes place on the negatively poled $CrO_2$−PTO surface, but for the reasons described above, the binding energy is much smaller.

## ■ OUTLOOK AND CONCLUSIONS

The above theoretical results highlight the promise of this class of catalysts when operated in a cyclical fashion. However, cyclically switching the ferroelectric polarization is experimentally challenging. We mention some alternative ideas that may alleviate this difficulty. First, as Table 1 indicates, the $CrO_2$−PTO system has very similar behaviors in paraelectric and positive polarizations. Thus, one can cycle between paraelectric and negative polarizations. This can be achieved by using temperature. As long as the material can be engineered to prefer negative polarization at low temperatures, raising the temperature near the Curie point should render the system paraelectric. In this scenario, the rate-limiting step in simultaneous $NO_x$ direct decomposition and CO oxidation is NO dissociation on the paraelectric surface with a 1.6 eV barrier, which is still reasonably low, given that we are operating near the Curie temperature (Curie temperature of bulk $PbZr_xTi_{1-x}O_3$ can be higher than 600 K[99,100]). Second, as described above, $CrO_2$−PTO shows a strong magnetoelectric effect so that one could employ magnetic fields

to switch the polarization.[101] Third, ferroelectric thin films can sport adjacent domains of opposite out-of-plane polarization whose size and pattern can be experimentally controlled and preserved up to high temperatures (785 °C).[102−104] Under appropriate conditions, one can imagine that reactions proceed on the positive domains and the buildup of products eventually causes their diffusion onto the adjacent negatively poled regions, where the remainder of the reactions take place. This approach requires control over the domain structure and reaction conditions but avoids the need to actually cycle the polarization. These suggestions are simply provided as potential avenues of exploration; whether and how the polarization should be cycled is fundamentally an experimental challenge. We hope this work will stimulate experimental interest in addressing these problems to study and exploit the potential of these catalytic oxide monolayers on ferroelectrics.

In conclusion, we have described catalytic systems consisting of a transition metal oxide monolayer on a ferroelectric oxide substrate. We propose that cycling between positive and negative polarization states of the ferroelectric makes these monolayers display catalytic behaviors that avoid the familiar compromises stemming from the Sabatier principle. A $CrO_2$ monolayer is an optimized choice for simultaneous $NO_x$ direct decomposition (a long-standing challenge in the automotive industry) and CO oxidation. Moreover, this system has tolerance toward sulfur and water poisoning. In addition to promising surface chemistry, $CrO_2$−PTO shows interesting magnetic and structural features, including magnetoelectric effects and major surface reconstructions in negative polarization. We also show that inserting $SrTiO_3$ buffer layers between the ferroelectric $PbTiO_3$ and the monolayer helps the monolayer wet the surface and avoid transition metal interdiffusion while not modifying the desirable surface chemistry. The scheme described in this work is general and, in principle, can be applied to and optimized for other chemical reactions. If experimentally feasible, this method can expand the range of catalytically active elements to those that are not conventionally considered for catalysis and might be more effective and economical, for example, Cr instead of canonical precious metal catalysts for simultaneous $NO_x$ direct decomposition and CO oxidation.

## ■ COMPUTATIONAL METHODS

We perform first-principles spin-polarized density functional theory (DFT) calculations[105,106] with plane-wave basis set using the Quantum Espresso software[107] and ultrasoft pseudopotentials.[108−110] We use $PbTiO_3$ (PTO) as the oxide ferroelectric and employ a slab geometry with the (001) direction for the surface normal and the polarization axis. We introduce at least 15 Å of vacuum on top of the surface in our unit cell. A dipole correction in the center of the vacuum is used to eliminate the artificial electrical field and the unphysical dipole−dipole interactions among the copies of the slab in the $z$ direction.[111] We use a kinetic energy cut-off for wave functions ($E_{cut}$) equal to 30 Ry, and a sampling for k space equivalent to $8 \times 8 \times 8$ sampling for a $1 \times 1$ cell. The smearing scheme for the Kohn−Sham orbitals' occupations is the cold smearing of Marzari and Vanderbilt with a temperature equal to 2 $mRy/k_B$.[112] All convergence parameters are chosen to yield binding energies better than 0.1 eV.

We use a standard method whereby a few layers of Pt are placed on the bottom PTO surface to create an electrode and a large density of states at the Fermi level. This simulates an electron reservoir that exists in a realistic system with a thick ferroelectric film.[15,45,113,114] It should be noted that the Pt layers

have a small enough lattice mismatch (<4%) with the PTO slab so as not to introduce any artificial interface effect on the bottom PTO surface. We fix the structure of the second, third, and fourth atomic layers of $PbTiO_3$ on top of the Pt electrode to their bulk values to help simulate the mechanical boundary conditions appropriate to a thick $PbTiO_3$ film; this leads to reasonable computational expenses and sizes of the simulation cells.[15,114−118]

Our tabulated results employ the PW91 GGA exchange-correlation (XC) functional,[119,120] but changing the XC functional to PBE GGA changes the binding energies by <15%, and this does not affect our main results and conclusions. We have also performed extensive DFT+U calculations of our surface systems as tabulated in the Supporting Information. However, the physically appropriate value of the Hubbard U parameter for both $CrO_2$−PTO and $RuO_2$−PTO systems is quite small (i.e., weak electronic correlations). Hence, our GGA results should be in better agreement with experiment than GGA +U results with moderate or large U values.

In more detail, in DFT+U theory, U is a semiempirical parameter typically determined by comparing computed results with experiments and choosing the U that yields the best agreement.[121−126] In our case, the closest experimentally available systems are are $CrO_2$ and $RuO_2$. In 2005, Toropova et al. showed that $CrO_2$ is, in fact, a weakly correlated material, and even relatively small values of 1−2 eV for U fail to describe its magnetic properties correctly.[126] We have also confirmed this in our own U = 0 GGA calculations for $CrO_2$, which we find to be a half metallic ferromagnetic material with 2 $\mu_B$ per Cr in the rutile structure with lattice parameters $a$ = 4.43 Å and $c/a$ = 0.6587, which is in excellent agreement with experimental values.[127] The agreement of the computed structural properties with experiment systematically worsens as U is increased in our GGA+U calculations. Next, $RuO_2$ (110) surface chemistry has been the subject of numerous theoretical and experimental studies.[51,52,128−130] It has been shown that binding energies calculated by GGA are in very good agreement with the experimentally observed values.[51] We find the same to be true and that increasing U systematically worsens the agreement. Separately, we have used the first-principles linear response approach[131] to estimate U and find values of 3.6 and 4.7 eV for $CrO_2$ and $RuO_2$, respectively. Unfortunately, these large U values do not provide the best agreement with available experiments. Hence, we conclude that using U = 0 for both the $RuO_2$−PTO and $CrO_2$−PTO systems should yield the most realistic results for binding energies.

To benchmark our PW91 GGA results for binding energies, we compare our results for CO and NO binding to $RuO_2$(110) with experimental and theoretical values in the literature.[51] For 1 ML CO adsorption, we find a binding energy of 1.3 eV, which is in good agreement with the values 1.0 and 1.18 eV obtained by experiment and PBE GGA, respectively. For 1 ML NO adsorption, we find a binding energy of 1.7 eV, which is in good agreement with the values 1.34 and 1.61 eV obtained by experiment and PBE GGA, respectively.[51]

To calculate the energy barriers between local minima, we use the nudged elastic band (NEB) method with climbing images,[132−138] variable elastic constants ($k_{max}/k_{min}$ = 3), and 6−8 images. In our NEB calculations, we permit the atoms in the top 2−3 atomic layers of the surface to move and fix the positions of all remaining atoms. We have checked that this introduces an error of no more than 0.1 eV in the energy barriers.

The shaded regions of the densities of states in Figures 3 and 4e highlight the Cr 3d- and Ru 4d-dominated conduction bands of the systems. Focusing on the Ru case as an example, the lower edge of the conduction band is clearly visible because the Ru 4d density of states shows a sudden and steep increase. We find that locating the precise numerical value for the lower edge is subject to a small uncertainty of ±0.2 eV. This, in turn, leads to an uncertainty of no more than ±0.02 eV for the center of the conduction band and ±0.04 for the electron count per 1 × 1 cell on the surface. Similar results are found for Cr.

## ■ ASSOCIATED CONTENT

**ⓢ Supporting Information**

The Supporting Information is available free of charge on the ACS Publications website at DOI: 10.1021/acscatal.5b00507.

Further details on DFT and DFT+U calculations, structures, and transition metal oxide optimization process (PDF)

## ■ AUTHOR INFORMATION

**Corresponding Author**

*E-mail: arvin.kakekhani@yale.edu.

**Notes**

The authors declare no competing financial interest

## ■ REFERENCES

(1) Logadottir, A.; Rod, T. H.; Norskov, J. K.; Hammer, B.; Dahl, S.; Jacobsen, C. J. H. *J. Catal.* **2001**, *197*, 229−231.

(2) Norskov, J. K.; Bligaard, T.; Logadottir, A.; Bahn, S.; Hansen, L. B.; Bollinger, M.; Bengaard, H.; Hammer, B.; Sljivancanin, Z.; Mavrikakis, M.; Xu, Y.; Dahl, S.; Jacobsen, C. J. H. *J. Catal.* **2002**, *209*, 275−278.

(3) Chorkendorff, I.; Niemantsverdriet, J. W. *Concepts of Modern Catalysis and Kinetics*; John Wiley & Sons: New York, 2006.

(4) Norskov, J. K.; Bligaard, T.; Rossmeisl, J.; Christensen, C. H. *Nat. Chem.* **2009**, *1*, 37−46.

(5) Hammer, B.; Norskov, J. K. *Adv. Catal.* **2000**, *45*, 71−129.

(6) Hansgen, D. A.; Vlachos, D. G.; Chen, J. G. *Nat. Chem.* **2010**, *2*, 484−489.

(7) Mavrikakis, M. *Nat. Mater.* **2006**, *5*, 847−848.

(8) Greeley, J.; Stephens, I. E. L.; Bondarenko, A. S.; Johansson, T. P.; Hansen, H. A.; Jaramillo, T. F.; Rossmeisl, J.; Chorkendorff, I.; Norskov, J. K. *Nat. Chem.* **2009**, *1*, 552−556.

(9) Zhang, Y.; Kolmakov, A.; Chretien, S.; Metiu, H.; Moskovits, M. *Nano Lett.* **2004**, *4*, 403−407.

(10) Zhang, Y.; Kolmakov, A.; Lilach, Y.; Moskovits, M. *J. Phys. Chem. B* **2005**, *109*, 1923−1929.

(11) Sato, Y.; Takai, K.; Enoki, T. *Nano Lett.* **2011**, *11*, 3468−3475.

(12) Baeumer, C.; Saldana-Greco, D.; Martirez, J. M. P.; Rappe, A. M.; Shim, M.; Martin, L. W. *Nat. Commun.* **2015**, *6*, 1−1.

(13) Popescu, D. G.; Husanu, M. A.; Trupina, L.; Hrib, L.; Pintilie, L.; Barinov, A.; Lizzit, S.; Lacovig, P.; Teodorescu, C. M. *Phys. Chem. Chem. Phys.* **2015**, *17*, 509−520.

(14) Sanna, S.; Holscher, R.; Schmidt, W. G. *Appl. Surf. Sci.* **2014**, *301*, 70−78.

(15) Garrity, K.; Kakekhani, A.; Kolpak, A.; Ismail-Beigi, S. *Phys. Rev. B: Condens. Matter Mater. Phys.* **2013**, *88*, 045401.

(16) Kolpak, A. M.; Grinberg, I.; Rappe, A. M. *Phys. Rev. Lett.* **2007**, *98*, 166101.

(17) Yun, Y.; Pilet, N.; Schwarz, U. D.; Altman, E. I. *Surf. Sci.* **2009**, *603*, 3145−3154.

(18) Bharath, S. C.; Pearl, T. P. *Surf. Sci.* **2010**, *604*, 713−717.

(19) Kim, S.; Schoenberg, M. R.; Rappe, A. M. *Phys. Rev. Lett.* **2011**, *107*, 076102.

(20) Yokomichi, Y.; Nakayama, T.; Okada, O.; Yokoi, Y.; Takahashi, I.; Uchida, H.; Ishikawa, H.; Yamaguchi, R.; Matsui, H.; Yamabe, T. *Catal. Today* **1996**, *29*, 155−160.

(21) Falsig, H.; Bligaard, T.; Rass-Hansen, J.; Kustov, A. L.; Christensen, C. H.; Norskov, J. K. *Top. Catal.* **2007**, *45*, 117−120.

(22) Imanaka, N.; Masui, T. *Appl. Catal., A* **2012**, *431−432*, 1−8.

(23) Matsumoto, S. *Catal. Today* **2004**, *90*, 183−190.

(24) Liu, Z.-P.; Hu, P. *Top. Catal.* **2004**, *28*, 71−78.

(25) Jobson, E. *Top. Catal.* **2004**, *28*, 191−199.

(26) Twigg, M. V. *Appl. Catal., B* **2007**, *70*, 2−15.

(27) Kabin, K. S.; Muncrief, R. L.; Harold, M. P. *Catal. Today* **2004**, *96*, 79−89.

(28) Iwamoto, M.; Yahiro, H. *Catal. Today* **1994**, *22*, 5−18.

(29) Liu, Z.-P.; Hu, P. *Top. Catal.* **2004**, *28*, 71−78.

(30) Granger, P.; Parvulescu, V. I. *Chem. Rev.* **2011**, *111*, 3155−3207.

(31) Parravano, G. *J. Chem. Phys.* **1952**, *20*, 342−343.

(32) Yun, Y.; Altman, E. I. *J. Am. Chem. Soc.* **2007**, *129*, 15684−15689.

(33) Yun, Y.; Kampschulte, L.; Li, M.; Liao, D.; Altman, E. I. *J. Phys. Chem. C* **2007**, *111*, 13951−13956.

(34) Inoue, Y.; Sato, K.; Sato, K.; Miyama, H. *J. Phys. Chem.* **1986**, *90*, 2809−2810.

(35) Park, S.; Lee, C. W.; Kang, M.-G.; Kim, S.; Kim, H. J.; Kwon, J. E.; Park, S. Y.; Kang, C.-Y.; Hong, K. S.; Nam, K. T. *Phys. Chem. Chem. Phys.* **2014**, *16*, 10408−10413.

(36) Inoue, Y.; Okamura, M.; Sato, K. *J. Phys. Chem.* **1985**, *89*, 5184−5187.

(37) Inoue, Y.; Yoshioka, I.; Sato, K. *J. Phys. Chem.* **1984**, *88*, 1148−1151.

(38) Garra, J.; Vohs, J. M.; Bonnell, D. A. *Surf. Sci.* **2009**, *603*, 1106−1114.

(39) Riefer, A.; Sanna, S.; Schmidt, W. G. *Phys. Rev. B: Condens. Matter Mater. Phys.* **2012**, *86*, 125410.

(40) Geneste, G.; Dkhil, B. *Phys. Rev. B: Condens. Matter Mater. Phys.* **2009**, *79*, 235420.

(41) Zhang, Z.; Sharma, P.; Borca, C. N.; Dowben, P. A.; Gruverman, A. *Appl. Phys. Lett.* **2010**, *97*, 243702.

(42) Zhang, Z.; Gonzalez, R.; Diaz, G.; Rosa, L. G.; Ketsman, I.; Zhang, X.; Sharma, P.; Gruverman, A.; Dowben, P. A. *J. Phys. Chem. C* **2011**, *115*, 13041−13046.

(43) Mi, Y.; Geneste, G.; Rault, J. E.; Mathieu, C.; Pancotti, A.; Barrett, N. *J. Phys.: Condens. Matter* **2012**, *24*, 275901.

(44) Rault, J. E.; Dionot, J.; Mathieu, C.; Feyer, V.; Schneider, C. M.; Geneste, G.; Barrett, N. *Phys. Rev. Lett.* **2013**, *111*, 127602.

(45) Lee, J. H.; Selloni, A. *Phys. Rev. Lett.* **2014**, *112*, 196102.

(46) Garrity, K.; Kolpak, A. M.; Ismail-Beigi, S.; Altman, E. I. *Adv. Mater.* **2010**, *22*, 2969−2973.

(47) Levchenko, S. V.; Rappe, A. M. *Phys. Rev. Lett.* **2008**, *100*, 256101.

(48) Martirez, J. M. P.; Morales, E. H.; Saidi, W. A.; Bonnell, D. A.; Rappe, A. M. *Phys. Rev. Lett.* **2012**, *109*, 256802.

(49) Yun, Y.; Li, M.; Liao, D.; Kampschulte, L.; Altman, E. I. *Surf. Sci.* **2007**, *601*, 4636−4647.

(50) Sanna, S.; Schmidt, W. G. *Phys. Rev. B: Condens. Matter Mater. Phys.* **2010**, *81*, 214116.

(51) Hong, S.; Rahman, T. S.; Jacobi, K.; Ertl, G. *J. Phys. Chem. C* **2007**, *111*, 12361−12368.

(52) Wang, Y.; Jacobi, K.; Ertl, G. *J. Phys. Chem. B* **2003**, *107*, 13918−13924.

(53) Eglitis, R. I.; Vanderbilt, D. *Phys. Rev. B: Condens. Matter Mater. Phys.* **2007**, *76*, 155439.

(54) Meyer, B.; Padilla, J.; Vanderbilt, D. *Faraday Discuss.* **1999**, *114*, 395−405.

(55) Amirnazmi, A.; Benson, J. E.; Boudart, M. *J. Catal.* **1973**, *30*, 55−65.

(56) Chuang, S. S. C.; Tan, C.-D. *J. Phys. Chem. B* **1997**, *101*, 3000−3004.

(57) Jiang, H.; Xing, L.; Czuprat, O.; Wang, H.; Schirrmeister, S.; Schiestel, T.; Caro, J. *Chem. Commun.* **2009**, 6738.

(58) Tofan, C.; Klvana, D.; Kirchnerova, J. *Appl. Catal., A* **2002**, *223*, 275−286.

(59) Tofan, C.; Klvana, D.; Kirchnerova, J. *Appl. Catal., A* **2002**, *226*, 225−240.

(60) Jiang, H.; Wang, H.; Liang, F.; Werth, S.; Schiestel, T.; Caro, J. *Angew. Chem., Int. Ed.* **2009**, *48*, 2983−2986.

(61) Reuter, K.; Scheffler, M. *Phys. Rev. Lett.* **2003**, *90*, 046103.

(62) Kolpak, A. M.; Ismail-Beigi, S. *Phys. Rev. B: Condens. Matter Mater. Phys.* **2011**, *83*, 165318.

(63) Matsumoto, S. i.; Ikeda, Y.; Suzuki, H.; Ogai, M.; Miyoshi, N. *Appl. Catal., B* **2000**, *25*, 115−124.

(64) Kolli, T.; Huuhtanen, M.; Hallikainen, A.; Kallinen, K.; Keiski, R. L. *Catal. Lett.* **2009**, *127*, 49−54.

(65) Keav, S.; Matam, S. K.; Ferri, D.; Weidenkaff, A. *Catalysts* **2014**, *4*, 226−255.

(66) Erkfeldt, S.; Skoglundh, M.; Larsson, M. In *Stud. Surf. Sci. Catal.*; Delmon, B., Froment, G. F., Eds.; Catalyst deactivation. Proceedings of the 8th International Symposium; Elsevier: New York, 1999; Vol. *126*; pp 211−218.

(67) Tzimpilis, E.; Moschoudis, N.; Stoukides, M.; Bekiaroglou, P. *Appl. Catal., B* **2009**, *87*, 9−17.

(68) Wang, X.; Qi, X.; Chen, Z.; Jiang, L.; Wang, R.; Wei, K. *J. Phys. Chem. C* **2014**, *118*, 13743−13751.

(69) Larsen, P. K.; Kampschoer, G. L. M.; Ulenaers, M. J. E.; Spierings, G. a. C. M.; Cuppens, R. *Appl. Phys. Lett.* **1991**, *59*, 611−613.

(70) Takashima, D.; Shuto, S.; Kunishima, I.; Takenaka, H.; Oowaki, Y.; Tanaka, S.-I. *IEEE J. Solid-State Circuits* **1999**, *34*, 1557−1563.

(71) Lemanov, V. V. *Ferroelectrics* **1999**, *226*, 133−146.

(72) Muller, K. A.; Burkard, H. *Phys. Rev. B: Condens. Matter Mater. Phys.* **1979**, *19*, 3593−3602.

(73) Haeni, J. H.; Irvin, P.; Chang, W.; Uecker, R.; Reiche, P.; Li, Y. L.; Choudhury, S.; Tian, W.; Hawley, M. E.; Craigo, B.; Tagantsev, A.; Pan, K.; Streiffer, X. Q.; Chen, S. K.; Kirchoefer, L. Q.; S, W.; Levy, J.; Schlom, D. G. *Nature* **2004**, *430*, 758−761.

(74) Hollmann, E.; Schubert, J.; Kutzner, R.; Wordenweber, R. *J. Appl. Phys.* **2009**, *105*, 114104.

(75) Zhou, J.-S.; Jin, C.-Q.; Long, Y.-W.; Yang, L.-X.; Goodenough, J. B. *Phys. Rev. Lett.* **2006**, *96*, 046408.

(76) Jones, C. W.; Battle, P. D.; Lightfoot, P.; Harrison, W. T. A. *Acta Crystallogr., Sect. C: Cryst. Struct. Commun.* **1989**, *45*, 365−367.

(77) Collaboration: Authors and editors of the volumes III/17H-17I-41E, In *Ternary Compounds, Organic Semiconductors*; Madelung, O., Rossler, U., Schulz, M., Eds.; Springer-Verlag: Berlin/Heidelberg, 2000; Vol. *41E*; pp 1−3.

(78) Madelung, O., Rossler, U., Schulz, M., Eds.; *Ternary Compounds, Organic Semiconductors*; Landolt-Bornstein − Group III Condensed Matter; Springer-Verlag: Berlin/Heidelberg, 2000; Vol. *41E*.

(79) Rodriguez, J. A.; Etxeberria, A.; Gonzalez, L.; Maiti, A. *J. Chem. Phys.* **2002**, *117*, 2699−2709.

(80) Heifets, E.; Eglitis, R. I.; Kotomin, E. A.; Maier, J.; Borstel, G. *Phys. Rev. B: Condens. Matter Mater. Phys.* **2001**, *64*, 235417.

(81) Koster, G.; Klein, L.; Siemons, W.; Rijnders, G.; Dodge, J. S.; Eom, C.-B.; Blank, D. H. A.; Beasley, M. R. *Rev. Mod. Phys.* **2012**, *84*, 253−298.

(82) Erdman, N.; Warschkow, O.; Asta, M.; Poeppelmeier, K. R.; Ellis, D. E.; Marks, L. D. *J. Am. Chem. Soc.* **2003**, *125*, 10050−10056.

(83) Shannon, R. D. *Acta Crystallogr., Sect. A: Cryst. Phys., Diffr., Theor. Gen. Crystallogr.* **1976**, *32*, 751−767.

(84) King-Smith, R. D.; Vanderbilt, D. *Phys. Rev. B: Condens. Matter Mater. Phys.* **1993**, *47*, 1651−1654.

(85) Resta, R.; Vanderbilt, D. Physics of Ferroelectrics. *Topics in Applied Physics*; Springer: Berlin Heidelberg, 2007; Vol. *105*; pp 31−68.

(86) Morioka, H.; Asano, G.; Oikawa, T.; Funakubo, H.; Saito, K. *Appl. Phys. Lett.* **2003**, *82*, 4761−4763.

(87) Morita, T.; Cho, Y. *Jpn. J. Appl. Phys.* **2004**, *43*, 6535.

(88) Chamberland, B. L.; Moeller, C. W. *J. Solid State Chem.* **1972**, *5*, 39−41.

(89) Jaya, S. M.; Jagadish, R.; Rao, R.; Asokamani, R. *Mod. Phys. Lett. B* **1992**, *06*, 103−112.

(90) Wang, B.-T.; Yin, W.; Li, W.-D.; Wang, F. *J. Appl. Phys.* **2012**, *111*, 013503.

(91) Garcia, V.; Bibes, M.; Bocher, L.; Valencia, S.; Kronast, F.; Crassous, A.; Moya, X.; Enouz-Vedrenne, S.; Gloter, A.; Imhoff, D.; Deranlot, C.; Mathur, N. D.; Fusil, S.; Bouzehouane, K.; Barthelemy, A. *Science* **2010**, *327*, 1106−1110.

(92) Duan, C.-G.; Jaswal, S. S.; Tsymbal, E. Y. *Phys. Rev. Lett.* **2006**, *97*, 047201.

(93) Stolichnov, I.; Riester, S. W. E.; Trodahl, H. J.; Setter, N.; Rushforth, A. W.; Edmonds, K. W.; Campion, R. P.; Foxon, C. T.; Gallagher, B. L.; Jungwirth, T. *Nat. Mater.* **2008**, *7*, 464−467.

(94) Mardana, A.; Ducharme, S.; Adenwalla, S. *Nano Lett.* **2011**, *11*, 3862−3867.

(95) Lukashev, P. V.; Burton, J. D.; Jaswal, S. S.; Tsymbal, E. Y. *J. Phys.: Condens. Matter* **2012**, *24*, 226003.

(96) Cai, T.; Ju, S.; Lee, J.; Sai, N.; Demkov, A. A.; Niu, Q.; Li, Z.; Shi, J.; Wang, E. *Phys. Rev. B: Condens. Matter Mater. Phys.* **2009**, *80*, 140415.

(97) Cherifi, R. O.; Ivanovskaya, V.; Phillips, L. C.; Zobelli, A.; Infante, I. C.; Jacquet, E.; Garcia, V.; Fusil, S.; Briddon, P. R.; Guiblin, N.; Mougin, A.; Unal, A. A.; Kronast, F.; Valencia, S.; Dkhil, B.; Barthelemy, A.; Bibes, M. *Nat. Mater.* **2014**, *13*, 345−351.

(98) Kokalj, A. *J. Mol. Graphics Modell.* **1999**, *17*, 176−179.

(99) Bellaiche, L.; Garcia, A.; Vanderbilt, D. *Phys. Rev. Lett.* **2000**, *84*, 5427−5430.

(100) Yamamoto, T. *Jpn. J. Appl. Phys.* **1996**, *35*, 5104.

(101) Kimura, T.; Goto, T.; Shintani, H.; Ishizaka, K.; Arima, T.; Tokura, Y. *Nature* **2003**, *426*, 55−58.

(102) Paruch, P.; Triscone, J.-M. *Appl. Phys. Lett.* **2006**, *88*, 162907.

(103) Gruverman, A.; Rodriguez, B. J.; Nemanich, R. J.; Kingon, A. I. *J. Appl. Phys.* **2002**, *92*, 2734−2739.

(104) Li, D.; Bonnell, D. A. *Annu. Rev. Mater. Res.* **2008**, *38*, 351−368.

(105) Kohn, W.; Becke, A. D.; Parr, R. G. *J. Phys. Chem.* **1996**, *100*, 12974−12980.

(106) Hohenberg, P.; Kohn, W. *Phys. Rev.* **1964**, *136*, B864−B871.

(107) Giannozzi, P.; Baroni, S.; Bonini, N.; Calandra, M.; Car, R.; Cavazzoni, C.; Ceresoli, D.; Chiarotti, G.; Cococcioni, M.; Dabo, I.; Dal Corso, A.; de Gironcoli, S.; Fabris, S.; Fratesi, G.; Gebauer, R.; Gerstmann, U.; Gougoussis, C.; Kokalj, A.; Lazzeri, M.; Martin-Samos, L.; Marzari, N.; Mauri, F.; Mazzarello, R.; Paolini, S.; Pasquarello, A.; Paulatto, L.; Sbraccia, C.; Scandolo, S.; Sclauzero, G.; Seitsonen, A.; Smogunov, A.; Umari, P.; Wentzcovitch, R. *J. Phys.: Condens. Matter* **2009**, *21*, 395502.

(108) Laasonen, K.; Car, R.; Lee, C.; Vanderbilt, D. *Phys. Rev. B: Condens. Matter Mater. Phys.* **1991**, *43*, 6796−6799.

(109) Vanderbilt, D. *Phys. Rev. B: Condens. Matter Mater. Phys.* **1990**, *41*, 7892−7895.

(110) Laasonen, K.; Pasquarello, A.; Car, R.; Lee, C.; Vanderbilt, D. *Phys. Rev. B: Condens. Matter Mater. Phys.* **1993**, *47*, 10142−10153.

(111) Bengtsson, L. *Phys. Rev. B: Condens. Matter Mater. Phys.* **1999**, *59*, 12301−12304.

(112) Marzari, N.; Vanderbilt, D.; De Vita, A.; Payne, M. C. *Phys. Rev. Lett.* **1999**, *82*, 3296−3299.

(113) Marshall, M. S. J.; Malashevich, A.; Disa, A. S.; Han, M.-G.; Chen, H.; Zhu, Y.; Ismail-Beigi, S.; Walker, F.; Ahn, C. *Phys. Rev. Appl.* **2014**, *2*, 051001.

(114) Kolpak, A. M.; Li, D.; Shao, R.; Rappe, A. M.; Bonnell, D. A. *Phys. Rev. Lett.* **2008**, *101*, 036102.

(115) Tripkovic, V.; Skulason, E.; Siahrostami, S.; Norskov, J. K.; Rossmeisl, J. *Electrochim. Acta* **2010**, *55*, 7975−7981.

(116) Hawkins, J. M.; Weaver, J. F.; Asthagiri, A. *Phys. Rev. B: Condens. Matter Mater. Phys.* **2009**, *79*, 125434.

(117) Yang, Y.; White, M. G.; Liu, P. *J. Phys. Chem. C* **2012**, *116*, 248−256.

(118) Wang, C.-C.; Yang, Y.-J.; Jiang, J.-C.; Tsai, D.-S.; Hsieh, H.-M. *J. Phys. Chem. C* **2009**, *113*, 17411−17417.

(119) Burke, K., Perdew, J. P., Wang, Y. In *Electronic Density Functional Theory*; Dobson, A. J. F., Vignale, P. G., Das, D. M. P., Eds.; Springer: New York, 1998; pp 81−111.

(120) Perdew, J. P.; Yue, W. *Phys. Rev. B: Condens. Matter Mater. Phys.* **1986**, *33*, 8800−8802.

(121) Nolan, M.; Parker, S. C.; Watson, G. W. *Phys. Chem. Chem. Phys.* **2006**, *8*, 216−218.

(122) Nolan, M.; Grigoleit, S.; Sayle, D. C.; Parker, S. C.; Watson, G. W. *Surf. Sci.* **2005**, *576*, 217−229.

(123) Nolan, M.; Parker, S. C.; Watson, G. W. *J. Phys. Chem. B* **2006**, *110*, 2256−2262.

(124) Morgan, B. J.; Watson, G. W. *J. Phys. Chem. C* **2009**, *113*, 7322−7328.

(125) Hu, Z.; Metiu, H. *J. Phys. Chem. C* **2011**, *115*, 5841−5845.

(126) Toropova, A.; Kotliar, G.; Savrasov, S. Y.; Oudovenko, V. S. *Phys. Rev. B: Condens. Matter Mater. Phys.* **2005**, *71*, 172403.

(127) Schwarz, K. *J. Phys. F: Met. Phys.* **1986**, *16*, L211.

(128) Wendt, S.; Knapp, M.; Over, H. *J. Am. Chem. Soc.* **2004**, *126*, 1537−1541.

(129) Over, H.; Kim, Y. D.; Seitsonen, A. P.; Wendt, S.; Lundgren, E.; Schmid, M.; Varga, P.; Morgante, A.; Ertl, G. *Science* **2000**, *287*, 1474−1476.

(130) Wang, J.; Fan, C. Y.; Jacobi, K.; Ertl, G. *J. Phys. Chem. B* **2002**, *106*, 3422−3427.

(131) Cococcioni, M.; de Gironcoli, S. *Phys. Rev. B: Condens. Matter Mater. Phys.* **2005**, *71*, 035105.

(132) Mills, G.; Jonsson, H. *Phys. Rev. Lett.* **1994**, *72*, 1124−1127.

(133) Mills, G.; Jonsson, H.; Schenter, G. K. *Surf. Sci.* **1995**, *324*, 305−337.

(134) Henkelman, G.; Uberuaga, B. P.; Jonsson, H. *J. Chem. Phys.* **2000**, *113*, 9901−9904.

(135) Getman, R. B.; Schneider, W. F. *ChemCatChem* **2010**, *2*, 1450−1460.

(136) Balakrishnan, N.; Joseph, B.; Bhethanabotla, V. R. *Appl. Catal., A* **2013**, *462−463*, 107−115.

(137) Henkelman, G.; Jonsson, H. *J. Chem. Phys.* **2000**, *113*, 9978−9985.

(138) Sheppard, D.; Terrell, R.; Henkelman, G. *J. Chem. Phys.* **2008**, *128*, 134106.